Microsc. Microanal., page 1 of 12
doi:10.1017/S1431927614013348

Microscopy AND Microanalysis

Room Temperature Synthesis of Cu_2O Nanospheres: Optical Properties and Thermal Behavior

Daniela Nunes,[1,*] Lídia Santos,[1] Paulo Duarte,[1] Ana Pimentel,[1] Joana V. Pinto,[1] Pedro Barquinha,[1] Patrícia A. Carvalho,[2] Elvira Fortunato,[1,*] and Rodrigo Martins[1,*]

[1]*Departamento de Ciência dos Materiais, CENIMAT/I3N, Faculdade de Ciências e Tecnologia (FCT) Universidade Nova de Lisboa and CEMOP-UNINOVA, 2829-516 Caparica, Portugal*
[2]*ICEMS, Instituto Superior Técnico, Universidade Técnica de Lisboa, Av. Rovisco Pais, 1049-001 Lisboa, Portugal*

Abstract: The present work reports a simple and easy wet chemistry synthesis of cuprous oxide (Cu_2O) nanospheres at room temperature without surfactants and using different precursors. Structural characterization was carried out by X-ray diffraction, transmission electron microscopy, and scanning electron microscopy coupled with focused ion beam and energy-dispersive X-ray spectroscopy. The optical band gaps were determined from diffuse reflectance spectroscopy. The photoluminescence behavior of the as-synthesized nanospheres showed significant differences depending on the precursors used. The Cu_2O nanospheres were constituted by aggregates of nanocrystals, in which an *on/off* emission behavior of each individual nanocrystal was identified during transmission electron microscopy observations. The thermal behavior of the Cu_2O nanospheres was investigated with *in situ* X-ray diffraction and differential scanning calorimetry experiments. Remarkable structural differences were observed for the nanospheres annealed in air, which turned into hollow spherical structures surrounded by outsized nanocrystals.

Key words: cuprous oxide, nanospheres, photoluminescence, cathodoluminescence, precursor effect, thermal behavior

Introduction

Optical and electrical properties of cuprous oxide (Cu_2O) are mainly controlled by intrinsic defects, such as copper and/or oxygen vacancies. Copper vacancies are believed to be the cause of the *p*-type semiconductor character of Cu_2O (Mittiga et al., 2006; Figueiredo et al., 2008), whereas an *n*-type character is observed when the density of oxygen vacancies is higher than that of copper vacancies (Heng et al., 2012).

Cu_2O typically exhibits a *p*-type semiconductor character, displaying a high optical absorption coefficient (Al-Ghamdi et al., 2012), bulk band gap of 2.0–2.17 eV (Deki et al., 1998; Hara et al., 1998; Heng et al., 2012), and suitable electrical properties (Balamurugan & Mehta, 2001). Owing to these unique intrinsic properties, Cu_2O is widely employed in optoelectronics, such as in solar cells (Garuthara & Siripala, 2006; Wei et al., 2012) with a theoretical conversion efficiency over 13% (Al-Ghamdi et al., 2012). However, the thermal stability of Cu_2O is a concern and, as a result, the temperature range for Cu_2O application in optoelectronic devices is limited and must be strictly scrutinized (Balamurugan & Mehta, 2001). In addition, Cu_2O has been proposed as a material for thin-film transistors (Figueiredo et al., 2009, 2013), electrodes in lithium ion batteries (Bijani et al., 2007), photocatalyst for the photochemical decomposition of water under visible light (Hara et al., 1998; He et al., 2005), glucose sensors (Zhou et al., 2014), biosensors (Zhu et al., 2008; Geng et al., 2011), and gas sensors (Zhang et al., 2006; Chen et al., 2012).

The optical properties of Cu_2O are largely dependent on the nanoparticle size and shape (Zhang & Wang, 2011), and several approaches have been reported to control the final Cu_2O micro/nanocrystal morphology, namely nanowires (Filipič & Cvelbar, 2012; Nunes et al., 2014), nanorods (Wei & Huo, 2010), nanocubes (Chang et al., 2013), octahedral crystals (Cao et al., 2009), nanospheres (Chen et al., 2012; Sun et al., 2012; Jiang et al., 2013), and hollow structures (Sui et al., 2009; Wang et al., 2011). The latter are interesting because of the low density, high specific surface area, and good permeation (Sui et al., 2009). Furthermore, Cu_2O micro/nanospheres are expected to exhibit high light-collection efficiency and fast motion of charge carriers, as well as large surface area (Hsu et al., 2012). The most common approaches to synthesize Cu_2O micro/nanospheres are template-directed and hydrothermal synthesis (Sui et al., 2009; Zhang & Wang, 2011; Hsu et al., 2012). However, lower cost production at room temperature of controlled oxide nanostructures is still sought.

The present work reports the production of Cu_2O nanospheres at room temperature through a simple and easy chemistry route without surfactants and using different precursors. Structural characterization of the nanospheres was carried out by X-ray diffraction (XRD), transmission electron microscopy (TEM), and scanning electron microscopy (SEM) coupled with focused ion beam (FIB) and energy-dispersive X-ray spectroscopy (EDS). The thermal

Received May 22, 2014; accepted September 17, 2014
*Corresponding authors. ddsn.gomes@campus.fct.unl.pt; emf@fct.unl.pt; rm@uninova.pt

stability of the nanospheres was evaluated through differential scanning calorimetry (DSC) experiments and *in situ* XRD. Optical properties were assessed through diffuse reflectance spectroscopy and photoluminescence (PL) studies.

Materials and Methods

Cu_2O nanospheres were synthesized via a wet chemical route at room temperature. Sigma-Aldrich (Sigma-Aldrich Corporation, St. Louis, MO, USA) reagents were used as-received without further purification. The copper precursors tested were: copper (II) acetate ($Cu(CH_3CO_2)_2$), copper (II) sulfate pentahydrate ($CuSO_4.5H_2O$), copper (II) chloride ($CuCl_2$), and copper (II) nitrate ($Cu(NO_3)_2$). In ordinary reactions, 0.4 g of each precursor were dissolved in 50 mL of de-ionized water under constant stirring. Afterwards, 0.4 g of sodium hydroxide (NaOH) was added forming a blue precipitate of $Cu(OH)_2$, followed by 50 μL of ethylenediamine (EDA–$C_2H_8N_2$–99%) that turned into a translucent royal blue solution, probably owing to the formation of $[Cu(OH)_4]^{2-}$. In fact, EDA plays an important role on the definition of the nanoparticle shape and size (Rathmell et al., 2010; Meng & Jin, 2011). Finally, 310 μL of a 2 M solution of hydrazine monohydrate ($N_2H_4.H_2O$–65%) was added, and the reaction mixture evolved from blue into green, then yellow, and finally orange, the color associated with formation of Cu_2O. The reactions took place without the presence of surfactants. A 15-min reaction time (after adding hydrazine) was set for all precursors tested.

The reactions involved in the Cu_2O nanosphere synthesis are proposed as follows (Sharma & Sharma, 2013):

$$Cu(CH_3CO_2)_2 \rightarrow Cu^{2+} + 2CH_3CO_2^{-}, \quad (1)$$

$$CuSO_4 \rightarrow Cu^{2+} + SO_4^{2-}, \quad (2)$$

$$CuCl_2 \rightarrow Cu^{2+} + 2Cl^{-}, \quad (3)$$

$$Cu(NO_3)_2 \rightarrow Cu^{2+} + 2NO_3^{-}, \quad (4)$$

then

$$Cu^{2+} + 2NaOH + 2H_2O \rightarrow \left[Cu(OH)_4\right]^{2-} + 2Na^{+} + 2H^{+}, \quad (5)$$

$$2\left[Cu(OH)_4\right]^{2-} + N_2H_4 \rightarrow Cu_2O + N_2 \uparrow + 3H_2O + 4OH^{-} + H_2 \uparrow . \quad (6)$$

The intermediate formation of $Cu(OH)_2$ is not represented in equation (5) owing to the immediate conversion into $[Cu(OH)_4]^{2-}$ after adding EDA.

The as-synthesized materials were subsequently centrifuged at 4,000 rpm, washed thoroughly with de-ionized water and isopropyl alcohol, and dried in vacuum for 1 h to prevent further oxidation before characterization.

SEM observations were carried out using a Carl Zeiss AURIGA CrossBeam (FIB-SEM) workstation (Carl Zeiss Microscopy GmbH, Oberkochen, Germany), equipped for EDS measurements. The diameter of 50 individual nanospheres were determined from SEM micrographs using ImageJ software (Schneider et al., 2012). For the FIB experiments, performed to observe the inner cross-section of individual nanospheres, Ga^{+} ions were accelerated to 30 kV at 2 pA and the etching depth was kept around 300 nm. A thin layer (~30 nm) of carbon was deposited on the material surface to minimize Ga contamination.

TEM observations were carried out with a Hitachi H8100 microscope (Hitachi High Technologies America, Inc., Dallas, TX, USA) operated at 200 kV and equipped with EDS. A drop of the sonicated dispersion was deposited onto 200-mesh copper grids covered with formvar and allowed to dry before observation. Cathodoluminescence (CL) images were obtained during TEM observation, and CL films were acquired with the recording times of 4.17 or 5.83 s (12 and 13 frames/s, respectively) (see Supplementary Material). The images were obtained at 0° tilt angle to avoid any specific diffraction condition. The size of individual nanocrystals was determined through dark-field images using CL, and the size of 20 nanocrystals exhibiting CL behavior was measured using ImageJ software (Schneider et al., 2012).

Supplementary Material

Supplementary Material can be found online. Please visit journals.cambridge.org/jid_MAM.

DSC measurements were carried out with a Simultaneous Thermal Analyser TGA-DSC-STA 449 F3 Jupiter (Netzsch-Gerätebau GmbH, Selb, Germany). Approximately 2 mg of the dried powder was loaded into an open Al crucible and heated from room temperature to 500°C with a heating rate of 10°C/min in air. The annealing treatments were carried out by heating ~100 mg of the dried powder in a Nabertherm furnace under atmospheric conditions for 1 h at temperatures in the 200–500°C range.

XRD experiments were performed using a PANalytical X'Pert PRO MPD diffractometer (PANalytical B.V., Almelo, The Netherlands) equipped with an X'Celerator detector and CuKα radiation. The XRD data were acquired in the 20–90° 2θ range with a step size of 0.05°. *In situ* XRD experiments have been carried out in an MRI chamber at atmospheric conditions using a Pt–Rh foil as the heating element. The *in situ* diffractograms were collected in the same 2θ range and at temperatures of 30, 100, 200, 250, 300, 350, 400, and 500°C. The material was kept at each temperature step for at least half an hour to allow stabilization and five consecutive scans were collected for inspection of structural modifications during this time. The temperature was increased at a rate of 5° C/min. For comparison, Cu, CuO, and Cu_2O diffractograms were simulated with PowderCell (Kraus & Nolze, 1996) using previously published crystallographic data (Pearson et al., 1985). The average crystallite size was determined through

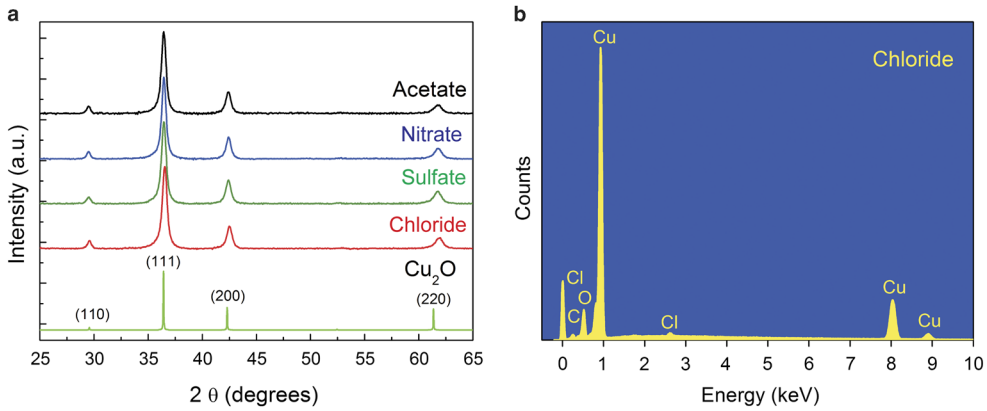

Figure 1. (**a**) X-ray diffractograms of Cu_2O nanospheres produced with the different precursors. (**b**) Energy-dispersive X-ray spectroscopy spectrum of Cu_2O particles synthesized with chloride as the precursor.

Scherrer's equation applied to the highest intensity low-angle Bragg reflection, Cu_2O_{111}.

The room temperature PL experiments were performed using a PerkinElmer LS-55 spectrophotometer (PerkinElmer, Inc., Waltham, MA, USA). The source of excitation was a Xenon lamp, and the excitation wavelengths tested were 488 and 555 nm. All measurements were carried out under equal excitation/detection conditions. The fluorescence images were obtained using an Axio Imager Z2m microscope (Carl Zeiss Microscopy GmbH, Göttingen, Germany) equipped with an HBO lamp, an EC Epiplan 50 × /0.7-NA HD-M27 objective lens, and an excitation filter in the green spectral region, 09 FITC filter cube (EX BP 450–490, BS FT 510, EM LP 515). The images were acquired using the Zen Black software, an AxioCam MRc camera (Carl Zeiss Microscopy GmbH, Göttingen, Germany) (RGB 1,388 × 1,040 pixels; 0.20 μm) and with an exposure time of 1 s.

Diffuse reflectance spectroscopy measurements of the dried powders were performed using a PerkinElmer lambda 950 UV/VIS/NIR spectrophotometer (PerkinElmer, Inc., Waltham, MA, USA) with a diffuse reflectance module (150 mm diameter integrating sphere, internally coated with Spectralon). Calibration of the system was achieved by using a "perfect" reflector disk (reflectance, $R = 1.00$) from Spectralon. The reflectance (R) was obtained from 250 to 1,200 nm.

Results and Discussion

Precursor Effects

Structural Characterization

In order to structurally characterize the as-synthesized materials, XRD and SEM experiments were carried out. XRD diffractograms of the Cu_2O nanospheres synthesized with the different precursors are presented in Figure 1. The peaks are fully assigned to Cu_2O and their broad width suggests the presence of small-sized particles. EDS analysis revealed that the Cu_2O material synthesized from $CuCl_2$ remained contaminated with Cl impurities after the cleaning procedure (Fig. 1b). Thus, the minimal Cu_2O_{111} peak shift observed is expected to be related to the ~1 at% Cl contamination as measured by EDS (Fultz & Howe, 2008; Lupan et al., 2010). The crystallite size calculated from Scherrer's equation is presented in Table 1. No significant differences can be observed for the different precursors.

SEM analysis (Fig. 2) shows that the synthesized structures present a nearly spherical shape and relatively smooth surface. The average nanosphere diameters for each precursor, as measured from SEM images, is presented in Figure 2 and Table 1. For the acetate and chloride precursors, the size distribution of the nanospheres is more symmetric and closer to a Gaussian curve, whereas nitrate and sulfate resulted in larger particles and higher size dispersion. The maximum Cu_2O nanosphere size detected was 850 nm for nitrate, while the minimum was around 100 nm for acetate.

FIB milling experiments were also carried out, which demonstrated that the nanospheres are aggregates of nanocrystals, justifying the values obtained by Scherrer's equation (Table 1). The internal structure is essentially compact although internal pores/voids were also detected (Figs. 3d, 4a). EDS maps were collected after the FIB milling experiments (Fig. 4) to attest for the homogeneous distribution of Cu and O in the Cu_2O nanospheres.

A bright/dark-field set of images and a diffraction pattern of an individual nanosphere are presented in Figure 3. The outer shell of the nanosphere displayed thinner/transparent areas (Fig. 3b) (Sharma & Bhatti, 2009) that confirmed the presence of individual nanocrystals as observed after FIB

Table 1. Cu_2O Crystallite Size Obtained with Scherrer's Equation and Average Nanosphere Diameters as Measured from Scanning Electron Microscopy Images for Different Precursors.

Precursors	Crystallite Size (nm)	Nanosphere Diameter (nm)
Acetate	14.2	479.1 ± 153.9
Nitrate	14.8	604.3 ± 146.0
Sulfate	15.9	487.4 ± 101.1
Chloride	15.3	533.3 ± 124.3

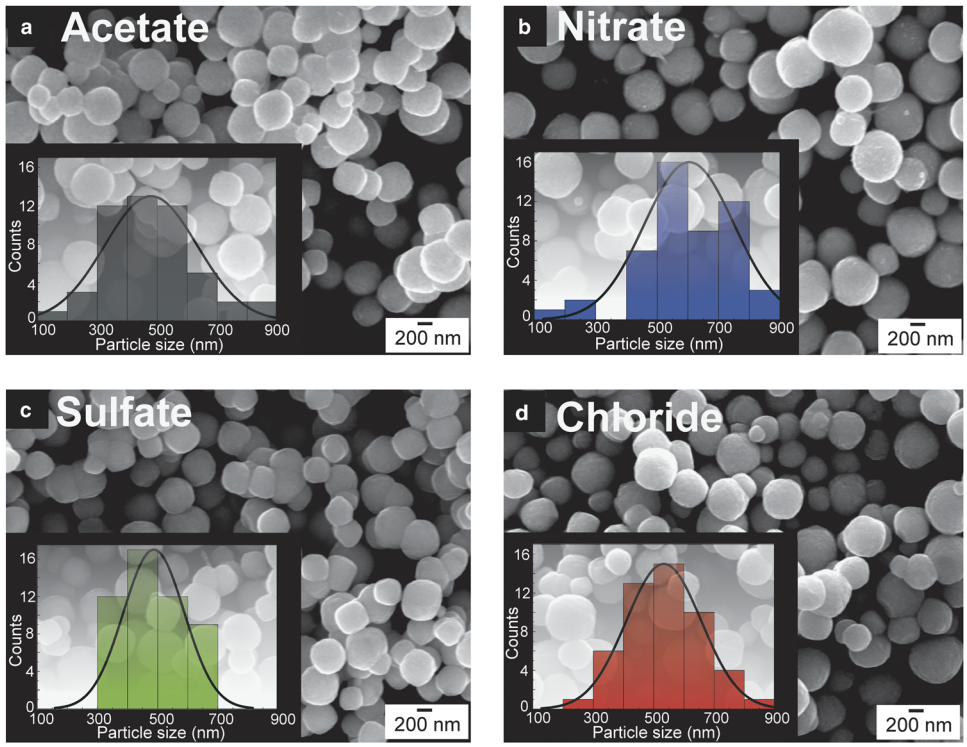

Figure 2. Scanning electron microscopy images of the Cu_2O nanospheres synthesized using (**a**) acetate, (**b**) nitrate, (**c**) sulfate, and (**d**) chloride as precursors. The insets show the size distribution of the Cu_2O nanospheres for each precursor tested.

milling. The diffraction pattern attested for the Cu_2O composition of the nanocrystals (as can be seen by the weak rings in Fig. 3c) and the diffuse halos confirmed the presence of amorphous domains, in agreement with a previous report (Zhang & Wang, 2011).

The aggregate structure was previously reported and justified through an Ostwald ripening process during formation of the nanospheres (Zhang & Wang, 2011). Initial Cu_2O nuclei are assembled through the reduction of Cu^{2+} ions by hydrazine [equation (6)], resulting in solid metastable spherical aggregates composed of nanocrystals and amorphous domains. Interior holes/voids appear within the solid nanospheres, as larger crystallites are essentially static whereas the smaller ones gradually dissolve into solution and recrystallize into larger ones. Therefore, the system equilibrium will shift toward structures that are thermodynamically more stable (Zhang & Wang, 2011).

Optical Characterization

Diffuse reflectance spectroscopy studies were carried out for the materials produced with different precursors. The remission function, $F(R)$, was calculated considering the Kubelka–Munk equation for optically thick materials, where the increase in thickness can no longer change the reflectance (R) experimentally determined (Kubelka & Munk, 1931; Yang & Kruse, 2004). The remission function is obtained by:

$$F(R) = \frac{(1-R)^2}{2R} = \frac{K}{S}, \tag{7}$$

where S and K are the scattering and absorption coefficients, respectively.

The optical band gap (E_g) of the semiconductor is related to the optical absorption coefficient (α) and the incident photon energy. The relation can be given as (Aydın et al., 2013):

$$\alpha h\nu = A(h\nu - E_g)^n, \tag{8}$$

where α is the linear absorption coefficient of the material, $h\nu$ the photon energy, A the proportionality constant, and n the constant exponent that determines the type of optical transition (in this case, for direct allowed transition, $n = ½$).

When the material scatters in a perfectly diffuse manner, the absorption coefficient K becomes equal to 2α. In this case, considering the scattering coefficient S as constant with respect to wavelength, and using the remission function in equation (8), the following expression is obtained:

$$[\mathrm{F}(R)\ h\nu]^2 = A_1\left(h\nu - E_g\right). \tag{9}$$

Therefore, the band gap can be determined by plotting the $[F(R)\ h\nu]^2$ against $h\nu$, and extracting the intersection of the extrapolation of the linear portion with 0 (Gu et al., 2010). The band gaps were estimated to be 2.05, 2.12, 2.07, and 2.13 eV for acetate, sulfate, chloride, and nitrate, respectively (Fig. 5). No significant band gap differences were observed between the precursors tested, moreover, the evaluated band gaps are close to the direct band gap of bulk Cu_2O (2.0–2.17 eV) (Heng et al., 2012).

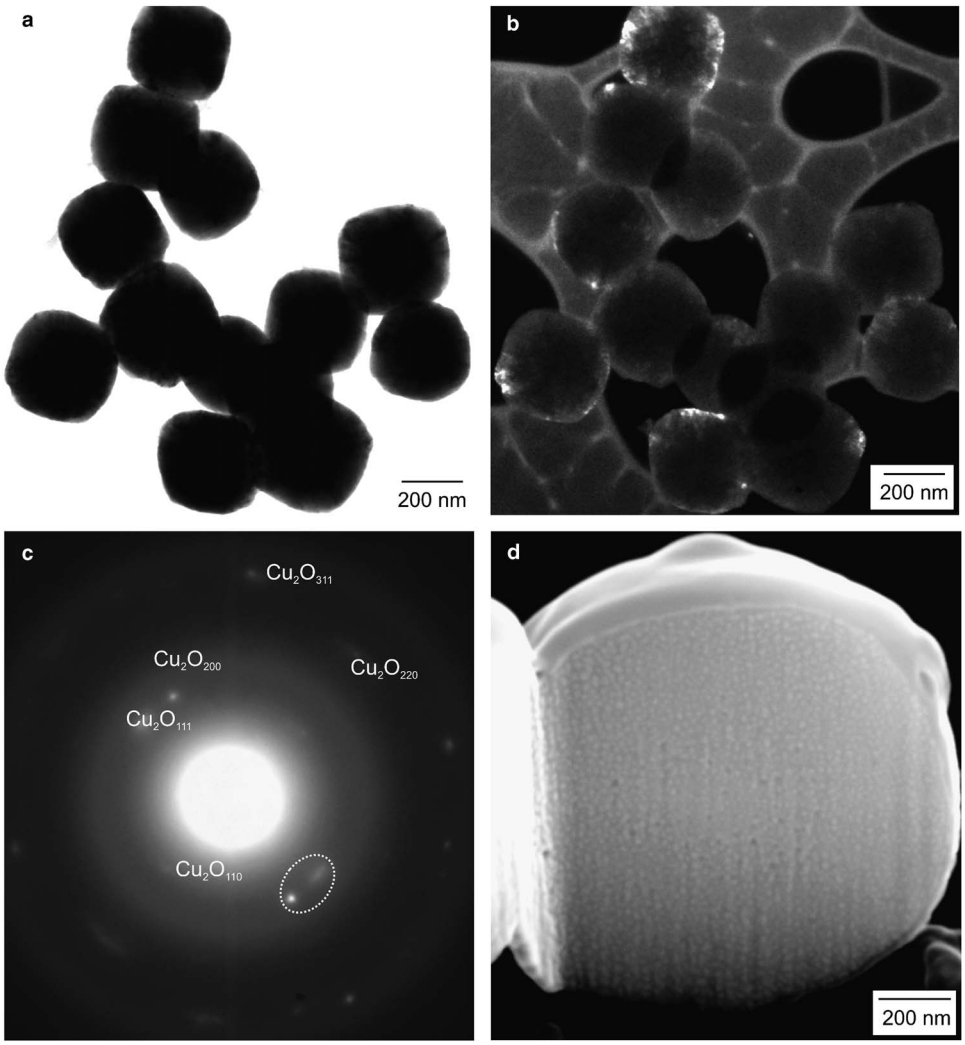

Figure 3. Transmission electron microscopy images of Cu_2O nanospheres synthesized with acetate, (**a**) bright-field, and (**b**) dark-field images. (**c**) Diffraction pattern of a single nanosphere, where the reflections used for dark-field images are circled, and (**d**) scanning electron microscopy image of a nanosphere after focused ion beam milling.

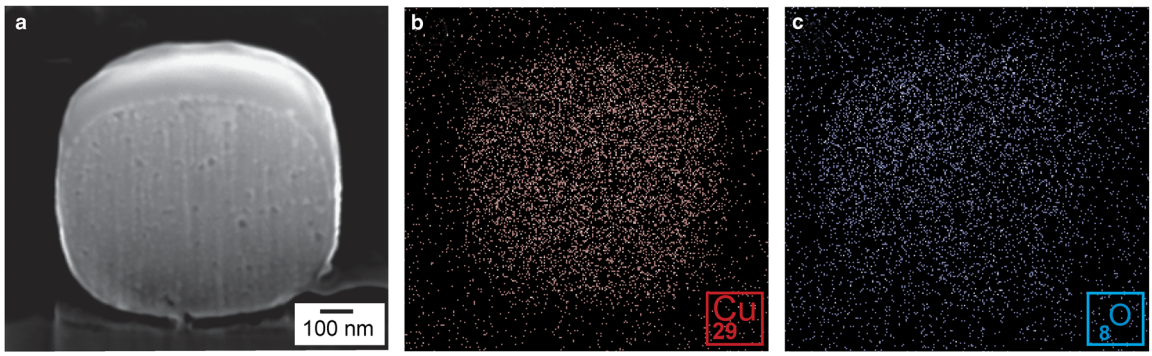

Figure 4. (**a**) Scanning electron microscopy image of a Cu_2O nanosphere synthesized with acetate and after focused ion beam milling. The corresponding X-ray maps for Cu (**b**) and O (**c**) are presented.

A multi-peaked feature can be observed in the remission function spectra for all the Cu_2O materials produced (see inset in Fig. 5). This behavior has been previously observed for similar Cu_2O solid aggregated nanospheres, and attributed to light scattering at the Mie resonances of the particles (Zhang & Wang, 2011). The direct comparison between the absorption and diffuse reflectance spectra is consistent, moreover, it has been reported that estimation of

band gaps through the latter method results in very accurate values (Morales et al., 2007).

Photoabsorption on a semiconductor requires higher energy to the photons (above its band gap), which results in an excited state. The excitation of an electron induces selective transitions from the valence band to higher energy states leaving holes, consequently the excited electrons will fulfill singular exciton energy levels close to the conduction band, generating an electron-hole pair (Karabudak et al., 2012). On the other hand, in PL, the electron-hole pair created by the photon absorption undergoes the recombination and emission of a luminescent photon (Gfroerer, 2000). Hence, considering the same kind of band gap states governing the recombination mechanism in all the materials, it is expected that the one having the lowest band gap presents the highest emission efficiency.

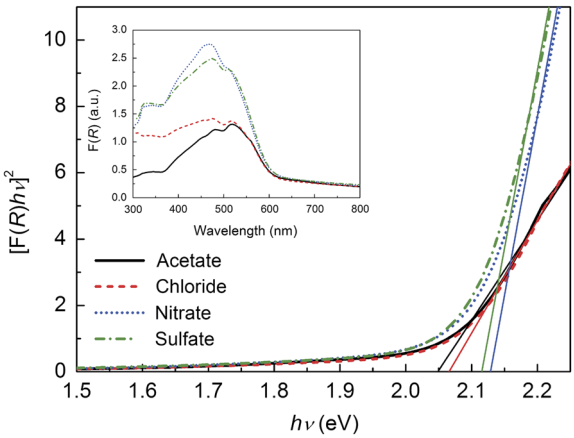

Figure 5. $[F(R)\ h\nu]^2$ variation versus photon energy $h\nu$. The inset shows remission function spectra regarding the precursors tested.

Cu_2O materials generally present significant luminescence, in which the PL spectra of Cu_2O crystals is originated by photoinduced electron-hole recombination or intrinsic defects (Heng et al., 2012). A decrease in the PL intensity usually suggests a recombination rate decrease, which is associated with an enhanced charge separation efficiency of photoinduced electrons and holes (Zhang, 2013). Figure 6 exhibits the room temperature PL spectra of the Cu_2O nanospheres synthesized with different precursors.

In all the studied materials, the emission intensity decreased with the increase in excitation wavelength, as previously reported (Djurišić et al., 2006). However, equal intensity trends were observed for both 488 and 555 nm excitation wavelengths. No PL band shift was observed comparing the precursors tested in agreement to the tendency followed by the remission spectra (see inset in Fig. 5) (Lupan et al., 2010).

The small PL band at 587 nm, corresponding to a band gap value of 2.11 eV, is attributed to the exciton emission of Cu_2O (Jana & Biswas, 1997; Ito et al., 1998; Vila et al., 2010) and the intense PL band at 732 nm (1.69 eV) may be assigned to the emission of multiple defect centers (Wu et al., 2006). Previously, the luminescence band detected at ~720 nm has been attributed to the presence of oxygen vacancies (V_O band) (Ito et al., 1998; Wang et al., 2014*b*), however, the origin of this defect peak is questionable and requires further clarification.

The behavior of both the PL bands observed in Figure 6 has been previously reported, in which materials with high density of defects, and exhibiting an intense defect-related emission PL band, presented almost an invisible exciton emission near the Cu_2O band gap region (Gu & Wang, 2010). Thus, Cu_2O nanospheres synthesized with acetate revealed a higher PL intensity when compared with the ones synthesized with other precursors, suggesting an enhanced density of defects that is assigned to recombination centers.

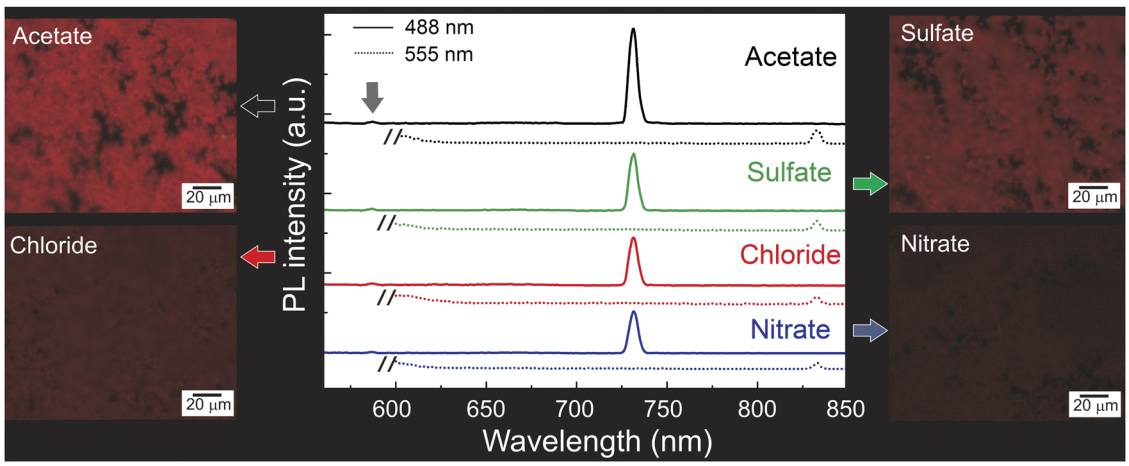

Figure 6. Photoluminescence spectra of the Cu_2O nanospheres synthesized with different precursors using the excitation wavelengths of 488 and 555 nm, without any peak normalization. The break feature at the 555 nm spectra is due to the appearance of the first order of the excitation band, and the arrow points to the exciton emission of Cu_2O. The fluorescence optical images are also presented, where no image treatment, e.g., contrast enhancement, has been performed.

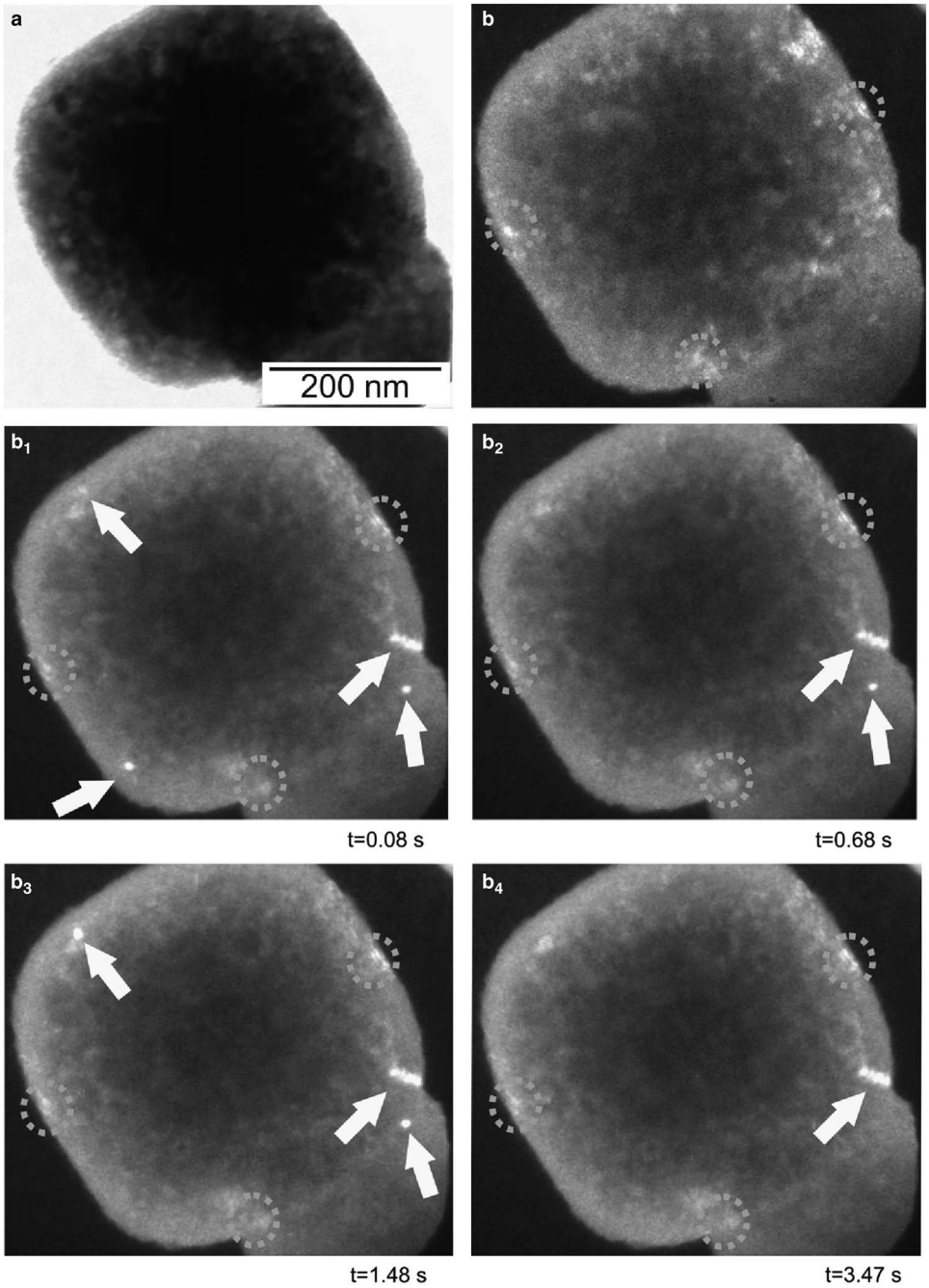

Figure 7. Transmission electron microscopy images of Cu_2O nanospheres synthesized with acetate. (**a**) Bright-field and (**b**) dark-field images. (**b_1-b_4**) Set of dark-field images showing a cathodoluminescence effect on individual grains during the transmission electron microscopy observations. The images are captured frames of a recorded video (see Supplementary Material). The arrows indicate the cathodoluminescent crystals. The dashed circles assign the diffraction contrast. The reflections used for the dark-field images were kept as indicated in Figure 3c.

This, together with the fact that the acetate-based materials show the lowest band gap (see also Fig. 5), makes them prone to exhibit the highest PL intensity, as depicted in Figure 6, which is in agreement with previous reports (Gangopadhyay et al., 2005; Cavalcante et al., 2012).

Fluorescence images show obvious disparities between the materials synthesized with the different precursors. In accordance to the PL analysis, synthesis with acetate resulted in more intense images.

CL signal emission in a semiconductor is a process induced by the incident electron beam, generating electron-hole pairs. These charge carriers diffuse and then recombine. The recombination of electrons and holes is then associated with the emission of photons (Abou-Ras et al., 2010). Live imaging was used to record the CL detected during TEM observations performed under on-axis dark-field conditions (Fig. 7 and Supplementary Material). Nanocrystals showing constant bright contrast strongly diffract the electron beam

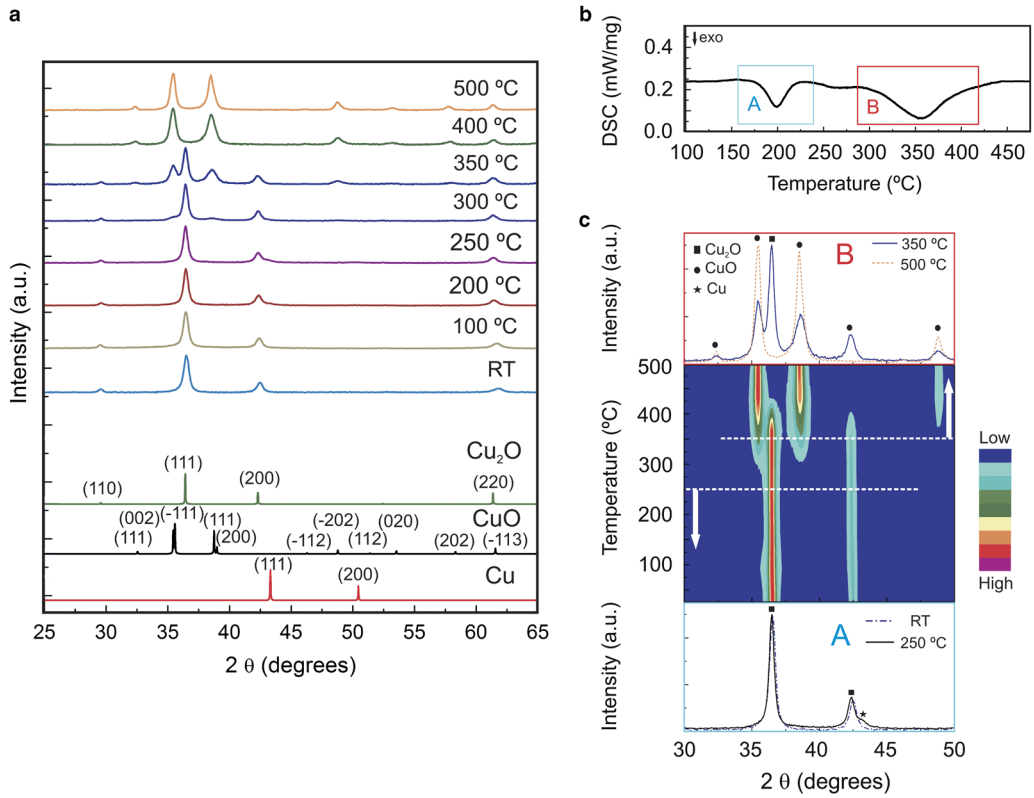

Figure 8. (**a**) *In situ* X-ray diffractograms of the Cu_2O nanospheres heat exposed up to 500°C. (**b**) Differential scanning calorimetry heating curve and (**c**) contour plot of XRD as a function of temperature, where the colors represent the XRD peak intensities. Bottom and top sections of (**c**) show XRD diffractograms for the temperature ranges corresponding to metallic Cu and CuO formation, A and B, respectively.

whereas the on/off emission process (blink) corresponds to the CL effect. It should be noted that sample tilting was not performed during the observations. Nanocrystals exhibiting diffraction contrast are indicated with dashed circles in Figures $7b_1$–$7b_4$, whereas the *on/off* emission behavior is indicated by arrows in the same images. The size of the nanocrystals exhibiting CL was estimated to be 14 ± 2.1 nm. The results are in good agreement with the crystallite size from Scherrer's equation (Table 1). The *on* emission state of single nanocrystals varied from ~0.7 to 1.5 s.

Thermal Analysis

The thermal behavior of the Cu_2O nanospheres was investigated using acetate as the precursor. As materials synthesized with acetate revealed a more intense PL emission, they were selected for a more detailed study in particular for its thermal behavior. Figure 8 shows the *in situ* XRD and DSC measurements, in which both techniques evidenced a stable chemistry up to about 150°C. However, the increase in temperature resulted in the appearance of metallic copper (see Figs. 8a, 8c; marked with A), thus the strong exothermic peak observed in DSC from 170 to 270°C was attributed to the Cu formation (Fig. 8b). From 300 to 500°C, the phase transformation of Cu_2O into CuO occurs (see Figs. 8a, 8c; marked with B). The strong exothermic peak in the 300–450°C range was attributed to the CuO conversion (Fig. 8b) (Hu et al., 2013).

The appearance of metallic Cu on Cu_2O materials annealed in air was unexpected. However, it has been reported during synthesis of Cu_2O nanoparticles, particularly after longer reaction times (Chen et al., 2003; Chang et al., 2004; Nakamura et al., 2008). Thus, the unique behavior observed at 200°C is thought to be related to the high surface energy of Cu_2O nanoparticles allowing the extraction of Cu^+ ions from the nanoparticles. However, with the increase in temperature, and probably owing to the high oxygen affinity that metallic copper possesses (Kevin et al., 2011), the predicted oxidation reaction $Cu_2O \rightarrow CuO$ (Firmansyah et al., 2009) takes place in detriment to metallic Cu formation. CuO starts to appear around 300°C in agreement with previous reports (Nakamura et al., 2008). Moreover, the appearance of the CuO phase is observed in the contour plot (Fig. 8c) where the $CuO_{002/-111}$ and $CuO_{200/111}$ peaks start to appear around 300°C.

At room temperature, relatively smooth Cu_2O nanospheres were clearly observed by SEM (Fig. 9a), as previously mentioned (Fig. 2). However, after annealing for 1 h at 200°C, the appearance of small voids on the surface was detected (Fig. 9b). At temperatures up to 300°C a rough surface with larger grains (30–90 nm) was observed (Fig. 9c), and at this point XRD and DSC experiments evidenced a mixture of Cu_2O and CuO. The increase in temperature resulted in the formation of hollow nanospheres, mostly of CuO, and the increase of grain size from 50 to 120 nm (Fig. 9d). At 500°C, the complete evolution into hollow CuO

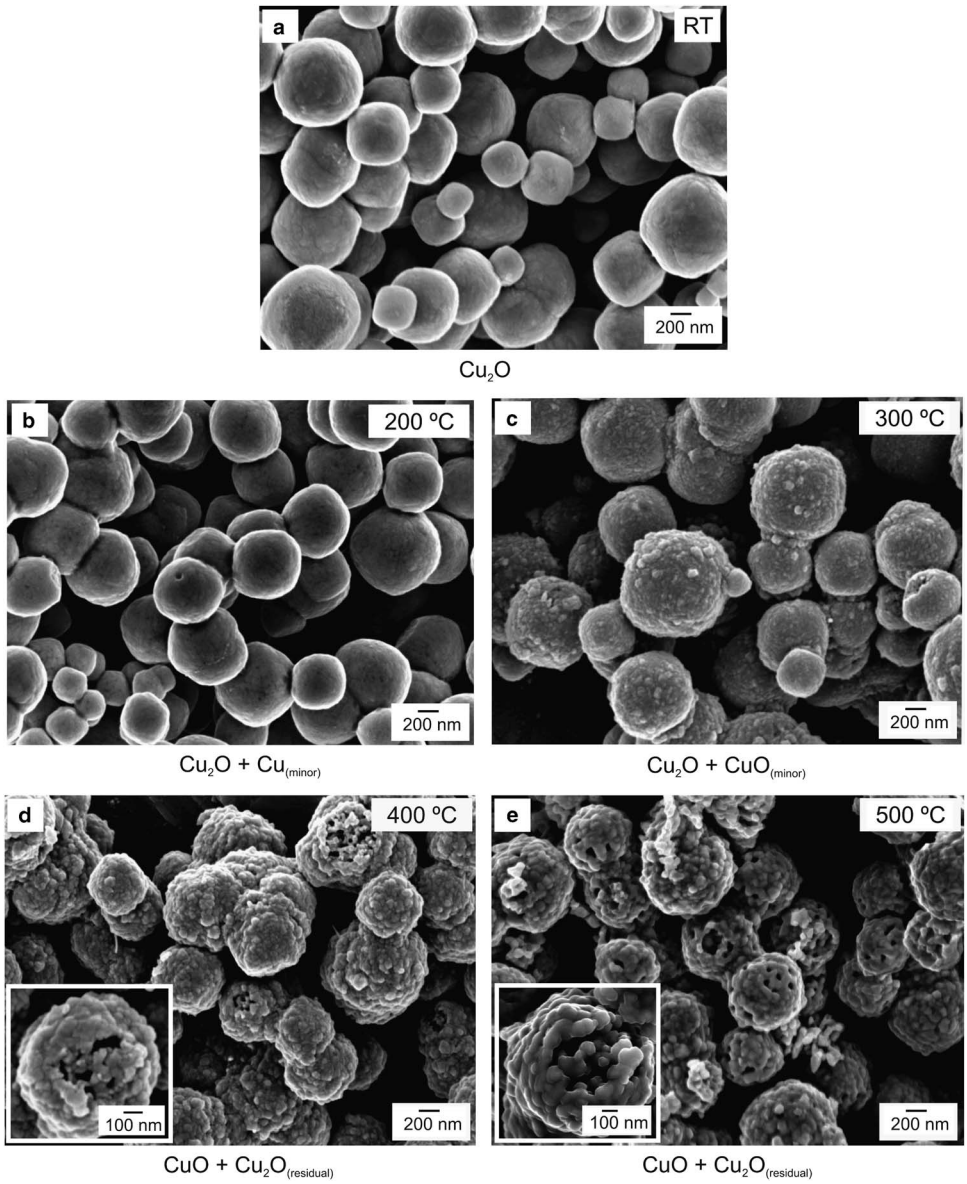

Figure 9. Scanning electron microscopy images of the Cu_2O nanospheres (**a**) at room temperature, (**b**) after annealing in air for 1 h at 200°C, (**c**) 300°C, (**d**) 400°C, and (**e**) 500°C. The insets in (**d** and **e**) show the evolution of the voids forming hollow nanospheres with the increase in annealing temperature.

nanospheres was observed (see the insets in Figs. 9d, 9e), together with collapsed structures. The breakage of structures is related to the strain induced on the whole structure during oxidation (Kevin et al., 2011).

Cu^+ is a highly active ion that is easily oxidized (Yang et al., 2006). The progression of the Cu_2O oxidation reaction is preceded by the appearance of CuO on the periphery of the former layer (Gonçalves et al., 2009; Korshunov & Il'in, 2009). The hollow structure of CuO nanospheres is speculated to be originated through the Kirkendall effect (Cho & Huh, 2009). The Kirkendall effect has been frequently used to explain the formation of hollow nanostructures (Fan et al., 2007), being based on a nonequilibrium mutual diffusion process with different diffusion rates (Hu et al., 2010). When the metallic ion of the oxide layer (fast-diffusing element) reacts with a slower diffusing one (oxygen), a large number of vacancies are created. Inside the small volume of the growing nanostructure, the vacancies coalesce into large voids that form the hollow nanostructures (Raidongia & Rao, 2008; Wang et al., 2014*a*). Moreover, the presence of initial voids on the nanospheres (see Figs. 3d, 4a) may also assist the faster formation of hollow structures during the oxidation.

The remission function spectra in Figure 10 exhibit differences between the as-synthesized and annealed materials, suggesting structural and compositional modifications (Zhang & Wang, 2011) in agreement with XRD, DSC, and SEM results (see Figs. 8, 9). Moreover, the evolution of the optical band gaps with annealing treatments revealed values of 2.05, 1.07, and 1.44 eV for the as-synthesized material and for the ones annealed at 200 and 500°C, respectively.

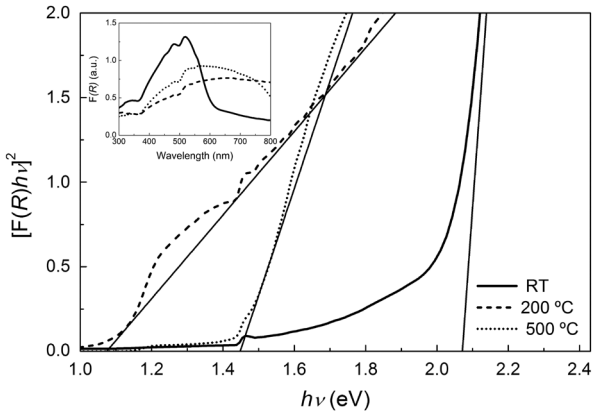

Figure 10. $[F(R)\ h\nu]^2$ variation versus photon energy $h\nu$. The inset shows remission function spectra comparing the as-synthesized Cu_2O nanospheres and after annealing in air for 1 h at 200 and 500°C.

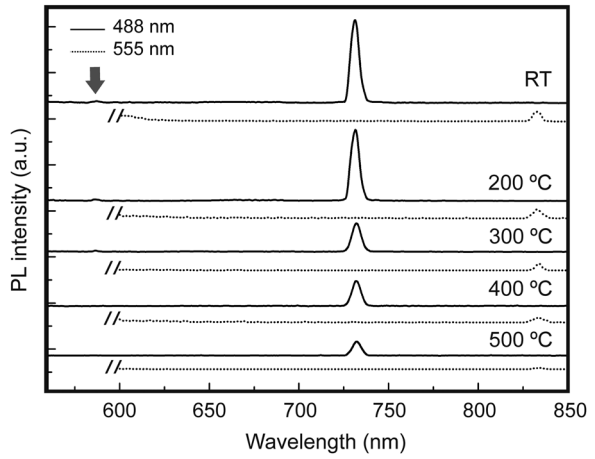

Figure 11. Photoluminescence spectra of the Cu_2O nanospheres after annealing treatments. The measurements were carried out with excitation wavelengths of 488 and 555 nm and the PL spectra were not normalized. The break feature at the 555 nm spectra is due to the appearance of the first order of the excitation band, and the arrow points to the exciton emission of Cu_2O.

The band gap of the initial Cu_2O nanospheres shifted to lower energies owing to the phase transitions observed on the materials annealed in air (Fig. 8). The presence of Cu was detected at 200°C, and the abrupt decrease in the band gap is related to the existence of pure metal on the material (Choudhury et al., 2013). With the increase in annealing temperature, CuO becomes the predominant phase. CuO displays the bulk band gap in the 1.30–1.7 eV range (Koffyberg & Benko, 1982; Serin et al., 2005; Kumar et al., 2013), thus the band gap (1.44 eV) of the hollow CuO nanospheres obtained at 500°C is in agreement with reported values.

Figure 11 shows the PL spectra of the annealed nanospheres up to 500°C. No PL band shift was observed after annealing in air for 1 h. However, the PL intensity was greatly degraded with the increase in annealing temperature, in agreement with previous reports (Shinagawa et al., 2013). The PL band at 587 nm (2.11 eV) associated to the exciton emission of Cu_2O disappears above 300°C, which coincides with the initial formation of CuO (see Fig. 8a). The presence of the 732 nm (1.69 eV) band that is associated with defects on Cu_2O decreases with the increase in annealing temperature. This behavior is attributed to two combined effects: the decrease in the defect concentration (Lupan et al., 2010) and the increase in the CuO phase. However, the PL results suggest that at temperatures up to 500°C, Cu_2O is present in a residual amount on the hollow CuO nanospheres.

Conclusions

The room temperature synthesis of Cu_2O nanospheres without surfactants and in the presence of different precursors was reported. No morphology discrepancy was detected regarding the precursors tested, however, a significant effect on particle size was observed. TEM showed that the Cu_2O nanospheres consisted of aggregates of nanocrystals, which was confirmed by FIB milling. The nanospheres synthesized with acetate displayed higher PL intensities, which suggests an enhanced density of defects. A CL effect occurred in individual nanocrystals during the TEM observations, with an evident *on/off* emission behavior. Thermal analysis of the nanospheres revealed that metallic copper formed up to 250°C, however, at 300°C, CuO starts to appear, and from 400°C or higher, CuO prevails. However, PL measurements suggested that up to 500°C, Cu_2O is still present in a residual amount on the hollow CuO nanospheres. The Cu_2O optical properties and the observed thermal stability up to ~150°C confirm the potential of this material for low cost optoelectronic device applications.

Acknowledgments

The work was supported by the Fundação para a Ciência e a Tecnologia, through the scholarship BPD/84215/2012 and the projects EXCL/CTM-NAN/0201/2012, PEst-C/CTM/LA0025/2013-14, and PEST-OE/CTM-UI0084/2011, as well as the European project CEOPS with the grant Agreement No. 309984, and by the European Research Council regarding the ERC 2008 Advanced Grant (INVISIBLE Contract No. 228144).

References

Abou-Ras, D., Jahn, U., Nichterwitz, M., Unold, T., Klaer, J. & Schock, H.W. (2010). Combined electron backscatter diffraction and cathodoluminescence measurements on stacks and thin-film solar cells. *J Appl Phys* **107**(1), 014311-1–014311-8.

Al-Ghamdi, A.A., Al-Hazmi, F., Al-Hartomy, O., El-Tantawy, F. & Yakuphanoglu, F. (2012). A novel synthesis and optical properties of cuprous oxide nano octahedrons via microwave hydrothermal route. *J Sol-Gel Sci Technol* **63**(1), 187–193.

Aydin, C., Benhaliliba, M., Al-Ghamdi, A., Gafer, Z., El-Tantawy, F. & Yakuphanoglu, F. (2013). Determination of optical band gap of $ZnO:ZnAl_2O_4$ composite semiconductor nanopowder materials by optical reflectance method. *J Electroceram* **31**(1–2), 265–270.

Balamurugan, B. & Mehta, B.R. (2001). Optical and structural properties of nanocrystalline copper oxide thin films prepared

by activated reactive evaporation. *Thin Solid Films* **396**(1–2), 90–96.

Bijani, S., Gabás, M., Martínez, L., Ramos-Barrado, J.R., Morales, J. & Sánchez, L. (2007). Nanostructured Cu_2O thin film electrodes prepared by electrodeposition for rechargeable lithium batteries. *Thin Solid Films* **515**(13), 5505–5511.

Cao, Y., Fan, J., Bai, L., Yuan, F. & Chen, Y. (2009). Morphology evolution of Cu_2O from octahedra to hollow structures. *Cryst Growth Des* **10**(1), 232–236.

Cavalcante, L., Longo, V., Sczancoski, J., Almeida, M., Batista, A., Varela, J., Orlandi, M.O., Longo, E. & Li, M.S. (2012). Electronic structure, growth mechanism and photoluminescence of $CaWO_4$ crystals. *Cryst Eng Comm* **14**(3), 853–868.

Chang, I.C., Chen, P.-C., Tsai, M.-C., Chen, T.-T., Yang, M.-H., Chiu, H.-T. & Lee, C.-Y. (2013). Large-scale synthesis of uniform Cu_2O nanocubes with tunable sizes by in-situ nucleation. *Cryst Eng Comm* **15**(13), 2363–2366.

Chang, Y., Teo, J.J. & Zeng, H.C. (2004). Formation of colloidal CuO nanocrystallites and their spherical aggregation and reductive transformation to hollow Cu_2O nanospheres. *Langmuir* **21**(3), 1074–1079.

Chen, W., Li, L., Peng, Q. & Li, Y. (2012). Polyol synthesis and chemical conversion of Cu_2O nanospheres. *Nano Res* **5**(5), 320–326.

Chen, Z.-Z., Shi, E.-W., Zheng, Y.-Q., Li, W.-J., Xiao, B. & Zhuang, J.-Y. (2003). Growth of hex-pod-like Cu_2O whisker under hydrothermal conditions. *J Cryst Growth* **249**(1–2), 294–300.

Cho, Y.S. & Huh, Y.D. (2009). Preparation of CuO hollow spheres by oxidation of Cu microspheres. *Bull Korean Chem Soc* **30**(6), 1410–1412.

Choudhury, B., Dey, M. & Choudhury, A. (2013). Defect generation, d-d transition, and band gap reduction in Cu-doped TiO_2 nanoparticles. *Int Nano Lett* **3**(1), 1–8.

Deki, S., Akamatsu, K., Yano, T., Mizuhata, M. & Kajinami, A. (1998). Preparation and characterization of copper(I) oxide nanoparticles dispersed in a polymer matrix. *J Mater Chem* **8**(8), 1865–1868.

Djurišić, A.B., Leung, Y.H., Tam, K.H., Ding, L., Ge, W.K., Chen, H.Y. & Gwo, S. (2006). Green, yellow, and orange defect emission from ZnO nanostructures: Influence of excitation wavelength. *Appl Phys Lett* **88**(10), 103107-1–103107-3.

Fan, H.J., Gçsele, U. & Zacharias, M. (2007). Formation of nanotubes and hollow nanoparticles based on Kirkendall and diffusion processes: A review. *Small* **3**(10), 1660–1671.

Figueiredo, V., Elangovan, E., Gonçalves, G., Barquinha, P., Pereira, L., Franco, N., Alves, E., Martins, R. & Fortunato, E. (2008). Effect of post-annealing on the properties of copper oxide thin films obtained from the oxidation of evaporated metallic copper. *Appl Surf Sci* **254**(13), 3949–3954.

Figueiredo, V., Elangovan, E., Gonçalves, G., Franco, N., Alves, E., Park, S.H.K., Martins, R. & Fortunato, E. (2009). Electrical, structural and optical characterization of copper oxide thin films as a function of post annealing temperature. *Phys Status Solidi (a)* **206**(9), 2143–2148.

Figueiredo, V., Pinto, J.V., Deuermeier, J., Barros, R., Alves, E., Martins, R. & Fortunato, E. (2013). P-type Cu_xO thin-film transistors produced by thermal oxidation. *J Display Technol* **9**(9), 735–740.

Filipič, G. & Cvelbar, U. (2012). Copper oxide nanowires: A review of growth. *Nanotechnology* **23**(19), 194001.

Firmansyah, D.A., Kim, T., Kim, S., Sullivan, K., Zachariah, M.R. & Lee, D. (2009). Crystalline phase reduction of cuprous oxide (Cu_2O) nanoparticles accompanied by a morphology change during ethanol-assisted spray pyrolysis. *Langmuir* **25**(12), 7063–7071.

Fultz, B. & Howe, J. (2008). Diffraction and the X-ray powder diffractometer. In *Transmission Electron Microscopy and Diffractometry of Materials*, pp. 1–59. Berlin, Heidelberg: Springer.

Gangopadhyay, P., Kesavamoorthy, R., Bera, S., Magudapathy, P., Nair, K., Panigrahi, B. & Narasimhan, S. (2005). Optical absorption and photoluminescence spectroscopy of the growth of silver nanoparticles. *Phys Rev Lett* **94**(4), 047403.

Garuthara, R. & Siripala, W. (2006). Photoluminescence characterization of polycrystalline n-type Cu_2O films. *J Lumin* **121**(1), 173–178.

Geng, B., Liu, J., Zhao, Y. & Wang, C. (2011). A room-temperature chemical route to homogeneous core-shell Cu_2O structures and their application in biosensors. *Cryst Eng Comm* **13**(2), 697–701.

Gfroerer, T.H. (2000). Photoluminescence in analysis of surfaces and interfaces. In *Encyclopedia of Analytical Chemistry*, Meyers, R.A. (Ed.), pp. 9209–9231. Chichester: John Wiley & Sons Ltd.

Gonçalves, A.M.B., Campos, L.C., Ferlauto, A.S. & Lacerda, R.G. (2009). On the growth and electrical characterization of CuO nanowires by thermal oxidation. *J Appl Phys* **106**(3), 034303-1–034303-5.

Gu, Q. & Wang, B. (2010). Correlation between structural defects and optical properties of Cu_2O nanowires grown by thermal oxidation. *arXiv Preprint arXiv:1012.5338*, 1–11.

Gu, Y.-E., Su, X., Du, Y. & Wang, C. (2010). Preparation of flower-like Cu_2O nanoparticles by pulse electrodeposition and their electrocatalytic application. *Appl Surf Sci* **256**(20), 5862–5866.

Hara, M., Kondo, T., Komoda, M., Ikeda, S., Kondo, J.N., Domen, K., Hara, M., Shinohara, K. & Tanaka, A. (1998). Cu_2O as a photocatalyst for overall water splitting under visible light irradiation. *Chem Commun* **3**, 357–358.

He, P., Shen, X. & Gao, H. (2005). Size-controlled preparation of Cu_2O octahedron nanocrystals and studies on their optical absorption. *J Colloid Interface Sci* **284**(2), 510–515.

Heng, B., Xiao, T., Tao, W., Hu, X., Chen, X., Wang, B., Sun, D. & Tang, Y. (2012). Zn doping-induced shape evolution of microcrystals: The case of cuprous oxide. *Cryst Growth Des* **12**(8), 3998–4005.

Hsu, Y.-K., Yu, C.-H., Chen, Y.-C. & Lin, Y.-G. (2012). Hierarchical Cu_2O photocathodes with nano/microspheres for solar hydrogen generation. *RSC Adv* **2**(32), 12455–12459.

Hu, L., Huang, Y., Zhang, F. & Chen, Q. (2013). CuO/Cu_2O composite hollow polyhedrons fabricated from metal-organic framework templates for lithium-ion battery anodes with a long cycling life. *Nanoscale* **5**(10), 4186–4190.

Hu, Y., Huang, X., Wang, K., Liu, J., Jiang, J., Ding, R., Ji, X. & Li, X. (2010). Kirkendall-effect-based growth of dendrite-shaped CuO hollow micro/nanostructures for lithium-ion battery anodes. *J Solid State Chem* **183**(3), 662–667.

Ito, T., Yamaguchi, H., Okabe, K. & Masumi, T. (1998). Single-crystal growth and characterization of Cu_2O and CuO. *J Mater Sci* **33**(14), 3555–3566.

Jana, S. & Biswas, P.K. (1997). Optical characterization of in-situ generated Cu_2O excitons in solution derived nano-zirconia film matrix. *Mater Lett* **32**(4), 263–270.

Jiang, L., You, T., Yin, P., Shang, Y., Zhang, D., Guo, L. & Yang, S. (2013). Surface-enhanced Raman scattering spectra of adsorbates on Cu_2O nanospheres: Charge-transfer and electromagnetic enhancement. *Nanoscale* **5**(7), 2784–2789.

Karabudak, E., Yuce, E., Schlautmann, S., Hansen, O., Mul, G. & Gardeniers, H. (2012). On the pathway of photoexcited electrons: Probing photon-to-electron and photon-to-phonon conversions in silicon by ATR-IR. *Phys Chem Chem Phys* **14**(31), 10882–10885.

Kevin, M., Ong, W.L., Lee, G.H. & Ho, G.W. (2011). Formation of hybrid structures: Copper oxide nanocrystals templated on ultralong copper nanowires for open network sensing at room temperature. *Nanotechnology* **22**(23), 235701.

Koffyberg, F.P. & Benko, F.A. (1982). A photoelectrochemical determination of the position of the conduction and valence band edges of p-type CuO. *J Appl Phys* **53**(2), 1173–1177.

Korshunov, A.V. & Il'in, A.P. (2009). Oxidation of copper nanopowders on heating in air. *Russ J Appl Chem* **82**(7), 1164–1171.

Kraus, W. & Nolze, G. (1996). POWDER CELL – A program for the representation and manipulation of crystal structures and calculation of the resulting X-ray powder patterns. *J Appl Cryst* **29**(3), 301–303.

Kubelka, P. & Munk, F. (1931). Ein beitrag zur optik der farbanstriche. *Z Tech Phys (Leipzig)* **12**, 593–601.

Kumar, V., Masudy-Panah, S., Tan, C.C., Wong, T.K.S., Chi, D.Z. & Dalapati, G.K. (2013). Copper oxide based low cost thin film solar cells. In *Nanoelectronics Conference, 2013 IEEE 5th International*, January 2013, Singapore: INEC, pp. 443–445.

Lupan, O., Pauporté, T., Chow, L., Viana, B., Pellé, F., Ono, L.K., Roldan Cuenya, B. & Heinrich, H. (2010). Effects of annealing on properties of ZnO thin films prepared by electrochemical deposition in chloride medium. *Appl Surf Sci* **256**(6), 1895–1907.

Meng, F. & Jin, S. (2011). The solution growth of copper nanowires and nanotubes is driven by screw dislocations. *Nano Lett* **12**(1), 234–239.

Mittiga, A., Salza, E., Sarto, F., Tucci, M. & Vasanthi, R. (2006). Heterojunction solar cell with 2% efficiency based on a Cu_2O substrate. *Appl Phys Lett* **88**(16), 163502.

Morales, A.E., Mora, E.S. & Pal, U. (2007). Use of diffuse reflectance spectroscopy for optical characterization of un-supported nanostructures. *Rev Mex Fıs S* **53**(5), 18–22.

Nakamura, R., Tokozakura, D., Lee, J.G., Mori, H. & Nakajima, H. (2008). Shrinking of hollow Cu_2O and NiO nanoparticles at high temperatures. *Acta Mater* **56**(18), 5276–5284.

Nunes, D., Pimentel, A., Barquinha, P., Carvalho, P.A., Fortunato, E. & Martins, R. (2014). Cu_2O polyhedral nanowires produced by microwave irradiation. *J Mater Chem C* **2**, 6097–6103.

Pearson, W.B., Villars, P. & Calvert, L.D. (1985). *Pearson's Handbook of Crystallographic Data for Intermetallic Phases*. Ohio: American Society for Metals.

Raidongia, K. & Rao, C.N.R. (2008). Study of the transformations of elemental nanowires to nanotubes of metal oxides and chalcogenides through the Kirkendall effect. *J Phys Chem C* **112**(35), 13366–13371.

Rathmell, A.R., Bergin, S.M., Hua, Y.-L., Li, Z.-Y. & Wiley, B.J. (2010). The growth mechanism of copper nanowires and their properties in flexible, transparent conducting films. *Adv Mater* **22**(32), 3558–3563.

Schneider, C.A., Rasband, W.S. & Eliceiri, K.W. (2012). NIH Image to ImageJ: 25 years of image analysis. *Nat Methods* **9**, 671–675.

Serin, N., Serin, T., Horzum, Ş. & Çelik, Y. (2005). Annealing effects on the properties of copper oxide thin films prepared by chemical deposition. *Semicond Sci Technol* **20**(5), 398–401.

Sharma, P. & Bhatti, H.S. (2009). Synthesis of fluorescent hollow and porous Cu_2O nanopolyhedras in the presence of poly(vinyl pyrrolidone). *Mater Chem Phys* **114**(2–3), 889–896.

Sharma, P. & Sharma, S.K. (2013). Microscopic investigations of Cu_2O nanostructures. *J Alloy Comp* **557**, 152–159.

Shinagawa, T., Onoda, M., Fariza, B.M., Sasano, J. & Izaki, M. (2013). Annealing effects and photoelectric properties of single-oriented Cu_2O films electrodeposited on Au(111)/Si(100) substrates. *J Mater Chem A* **1**(32), 9182–9188.

Sui, Y., Zhang, Y., Fu, W., Yang, H., Zhao, Q., Sun, P., Ma, D., Yuan, M., Li, Y. & Zou, G. (2009). Low-temperature template-free synthesis of Cu_2O hollow spheres. *J Cryst Growth* **311**(8), 2285–2290.

Sun, S., Zhang, X., Song, X., Liang, S., Wang, L. & Yang, Z. (2012). Bottom-up assembly of hierarchical Cu_2O nanospheres: Controllable synthesis, formation mechanism and enhanced photochemical activities. *Cryst Eng Comm* **14**(10), 3545–3553.

Vila, M., Diaz-Guerra, C. & Piqueras, J. (2010). Optical and magnetic properties of CuO nanowires grown by thermal oxidation. *J Phys D Appl Phys* **43**(13), 135403.

Wang, C.-M., Genc, A., Cheng, H., Pullan, L., Baer, D.R. & Bruemmer, S.M. (2014*a*). In-Situ TEM visualization of vacancy injection and chemical partition during oxidation of Ni-Cr nanoparticles. *Sci Rep* **4**, 1–6.

Wang, W., Tu, Y., Zhang, P. & Zhang, G. (2011). Surfactant-assisted synthesis of double-wall Cu_2O hollow spheres. *Cryst Eng Comm* **13**(6), 1838–1842.

Wang, Y., Miska, P., Pilloud, D., Horwat, D., Mücklich, F. & Pierson, J.F. (2014*b*). Transmittance enhancement and optical band gap widening of Cu_2O thin films after air annealing. *J Appl Phys* **115**(7), 073505-1–073505-5.

Wei, H.M., Gong, H.B., Chen, L., Zi, M. & Cao, B.Q. (2012). Photovoltaic efficiency enhancement of Cu_2O solar cells achieved by controlling homojunction orientation and surface microstructure. *J Phys Chem C* **116**(19), 10510–10515.

Wei, M. & Huo, J. (2010). Preparation of Cu_2O nanorods by a simple solvothermal method. *Mater Chem Phys* **121**(1–2), 291–294.

Wu, W.-T., Wang, Y., Shi, L., Pang, W., Zhu, Q., Xu, G. & Lu, F. (2006). Propeller-like multicomponent microstructures: Self-assemblies of nanoparticles of poly(vinyl alcohol)-coated Ag and/or Cu_2O. *J Phys Chem B* **110**(30), 14702–14708.

Yang, H., Ouyang, J., Tang, A., Xiao, Y., Li, X., Dong, X. & Yu, Y. (2006). Electrochemical synthesis and photocatalytic property of cuprous oxide nanoparticles. *Mater Res Bull* **41**(7), 1310–1318.

Yang, L. & Kruse, B. (2004). Revised Kubelka–Munk theory. I. Theory and application. *J Opt Soc Am A* **21**(10), 1933–1941.

Zhang, D. (2013). Synergetic effects of Cu_2O photocatalyst with titania and enhanced photoactivity under visible irradiation. *Acta Chim Slov* **6**(1), 141–149.

Zhang, J., Liu, J., Peng, Q., Wang, X. & Li, Y. (2006). Nearly monodisperse Cu_2O and CuO nanospheres: Preparation and applications for sensitive gas sensors. *Chem Mater* **18**(4), 867–871.

Zhang, L. & Wang, H. (2011). Cuprous oxide nanoshells with geometrically tunable optical properties. *ACS Nano* **5**(4), 3257–3267.

Zhou, D.-L., Feng, J.-J., Cai, L.-Y., Fang, Q.-X., Chen, J.-R. & Wang, A.-J. (2014). Facile synthesis of monodisperse porous Cu_2O nanospheres on reduced graphene oxide for non-enzymatic amperometric glucose sensing. *Electrochim Acta* **115**, 103–108.

Zhu, H., Wang, J. & Xu, G. (2008). Fast synthesis of Cu_2O hollow microspheres and their application in DNA biosensor of hepatitis B virus. *Cryst Growth Des* **9**(1), 633–638.